

Contents lists available at ScienceDirect

# Acta Materialia

journal homepage: www.elsevier.com/locate/actamat



# High performance high-power textured Mn/Cu-doped PIN-PMN-PT ceramics



Haoyang Leng<sup>a</sup>, Yongke Yan<sup>a,\*</sup>, Bo Wang<sup>a</sup>, Tiannan Yang<sup>a</sup>, Hairui Liu<sup>a</sup>, Xiaotian Li<sup>a</sup>, Rammohan Sriramdas<sup>a</sup>, Ke Wang<sup>a</sup>, Mark Fanton<sup>b</sup>, Richard J. Meyer<sup>b</sup>, Long-Qing Chen<sup>a,\*</sup>, Shashank Priya<sup>a,\*</sup>

- <sup>a</sup> Materials Research Institute, Department of Materials Science and Engineering, The Pennsylvania State University, University Park, Pennsylvania 16802, United States
- <sup>b</sup> Applied Research Laboratory, The Pennsylvania State University, State College, PA, 16801, USA

#### ARTICLE INFO

#### Article history: Received 17 November 2021 Revised 2 May 2022 Accepted 6 May 2022 Available online 8 May 2022

Keywords: Piezoelectric Crystallography Texturing Acceptor High power

#### ABSTRACT

Piezoelectric ceramics with combinatory soft and hard characteristics are highly desired for high-power applications. However, it remains grand challenge to achieve simultaneous presence of hard (e.g. high coercive field,  $E_c$ ; high mechanical quality factor,  $Q_m$ ) and soft (e.g. high piezoelectric constant, d; high electromechanical coupling factor, k) piezoelectric properties in piezoelectric ceramics since the mechanism controlling the hard behavior (pinned domain walls) will significantly reduce the soft behavior. Here, we address this grand challenge and demonstrate <001> textured MnO<sub>2</sub> and CuO co-doped Pb(In<sub>1/2</sub>Nb<sub>1/2</sub>)O<sub>3</sub>-Pb(Mg<sub>1/3</sub>Nb<sub>2/3</sub>)O<sub>3</sub>-PbTiO<sub>3</sub> (PIN-PMN-PT) ceramics exhibiting ultrahigh combined soft and hard piezoelectric properties ( $d_{33} = 713$  pC N<sup>-1</sup>,  $k_{31} = 0.52$ ,  $Q_m \approx 950$ ,  $E_c = 9.6$  kV cm<sup>-1</sup>, tan  $\delta = 0.45\%$ ). The outstanding electromechanical properties are explained by considering composition/phase selection, crystallographic anisotropy and defect engineering. Phase-field model in conjunction with high resolution electron microscopy and diffraction techniques is utilized to delineate the contributions arising from intrinsic piezoelectric response, domain dynamics, and local structural heterogeneity. These results will have significant impact in the development of high-power transducers and actuators.

© 2022 Acta Materialia Inc. Published by Elsevier Ltd. All rights reserved.

### 1. Introduction

Piezoelectric ceramics are widely utilized for transduction of mechanical energy into electrical energy and vice-versa [1,2]. A subset of tailored piezoelectric ceramics are utilized in high-power applications such as actuators, transformers, ultrasonic motors, and Langevin transducers [1,3,4]. Under high electric field (E) application near resonance, traditional piezoelectric materials will exhibit high magnitude of losses which is expressed as heat generation. To delay the degradation of piezoelectric behavior under high-power conditions, ceramics should exhibit a high mechanical quality factor  $Q_m$  and low dielectric loss factor A0, as heat generated is inversely proportional to mechanical quality factor and directly proportional to dielectric loss [5]. Large A0 is also beneficial in enhancing the displacement of piezoelectric element at resonance frequency [6,7]. In addition to A0, the high coercive field A1 is also

E-mail addresses: yxy355@psu.edu (Y. Yan), lqc3@psu.edu (L.-Q. Chen), sup103@psu.edu (S. Priya).

required to prevent the high-power material from depoling under high electric field. Further, high power piezoelectric ceramic should also possess high piezoelectric strain coefficient (d) to generate high vibration velocity ( $v_{\rm rms} \propto Q_m \cdot d$ ) and high electromechanical coupling factor (k) for effective electrical to mechanical energy conversion [5,8]. In summary, the high power piezoelectric ceramics should exhibit the hard properties (high  $Q_{\rm m}$ , high  $E_{\rm c}$ , low tan  $\delta$ ) and soft properties (high  $d_{33}$  and high k) simultaneously. However, achieving simultaneous hard and soft piezoelectric properties has long been a grand challenge. The hard properties are generally induced by acceptor doping, where acceptor ions (e.g. Mn<sup>2+</sup> or Mn<sup>3+</sup>) are substituted on B-site in a perovskite piezoelectric oxide. The aliovalent substitution of  $Mn^{2+}$  or  $Mn^{3+}$  cations on B-sites (e.g. Nb<sup>5+</sup> and Ti<sup>4+</sup>) will create the net negative charges on B-sites (e.g.  $Nb^{5+}$  and  $Ti^{4+}$ ) [9,10]. To maintain the charge balance, the positively charged oxygen vacancies  $V_{0}^{\cdot\cdot}$  will be created and the defect dipoles  $Mn_B^{\prime\prime}-V_O^{\cdot\cdot}$  will be formed. These defect dipoles are effective in pinning domain walls, which significantly reduces the piezoelectric properties of ceramics. Thus, despite decades of research and commercial development, high performance high-power piezoelectric ceramics are still hard to realize.

<sup>\*</sup> Corresponding authors.

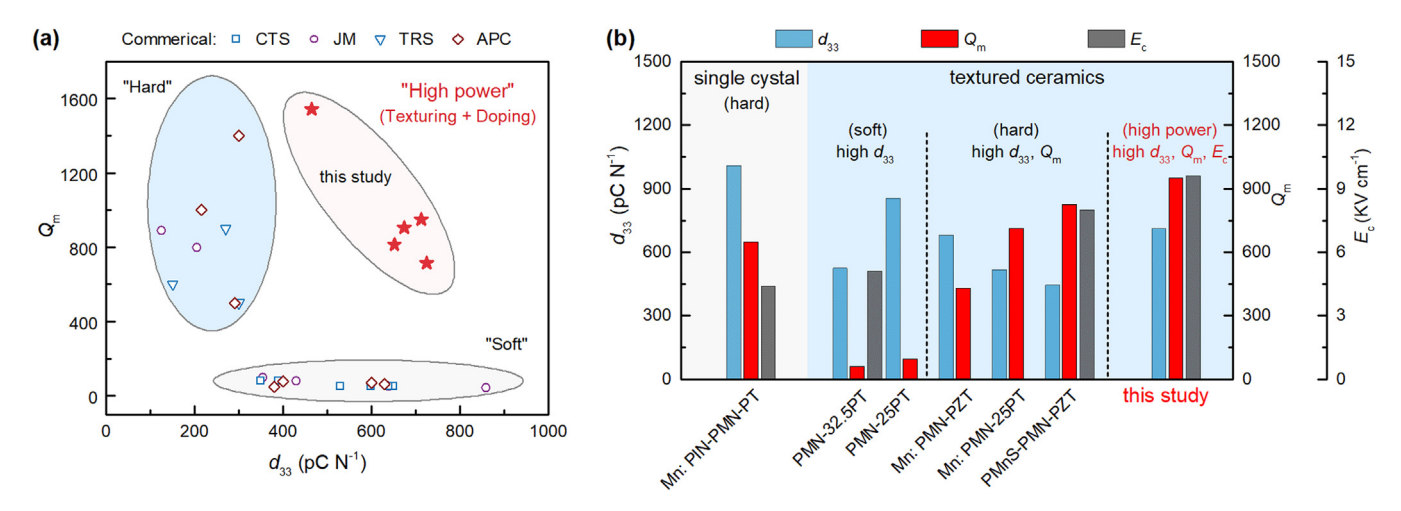


**Fig. 1. Comparison of high-power piezoelectric properties for different types piezoelectric ceramics.** (a) Mechanical quality factor  $Q_m$  vs piezoelectric strain constant  $d_{33}$  for high-power material developed in this study, and commercial hard and soft piezoelectric ceramics (References are included in Supplementary Information and different star points represent high-power piezoelectric properties of textured piezoelectric ceramics with different texturing degree). (b) Comparison of relevant parameters ( $d_{33}$ ,  $Q_m$ ,  $E_c$ ) in representative textured piezoelectric ceramics and Mn-doped PIN-PMN-PT single crystal [11,19–22].

One promising approach is to combine microstructural engineering and defect engineering to maximize the piezoelectric coefficient  $d_{33}$  and mechanical quality factor  $Q_{\rm m}$ . For example, a [001]-oriented rhombohedral Mn-doped PIN-PMN-PT single crystal has been reported to exhibit an excellent combination of high  $d_{33}$  ( $\sim$ 1009 pC N $^{-1}$ ) and high  $Q_{\rm m}$  ( $\sim$ 650) [11], which was attributed to the strong piezoelectric anisotropy and oxygen vacancy induced domain pinning. The [001]-oriented Mn-doped PIN-PMN-PT single crystal exhibited a high  $d_{33} \sim$ 1009 pC N $^{-1}$  while [111]-oriented crystal exhibited a low  $d_{33} \sim$  95 pC N $^{-1}$ , a difference of 1062% ( $d_{33[001]}/d_{33[111]}$ ), which clearly demonstrates the role of piezoelectric anisotropy [11]. There are some challenges in utilizing single crystals including high production cost, low coercive field ( $E_{\rm C}$ ), complexity in machining varying shapes and sizes, and smaller mechanical strength [12,13].

Prior studies have shown that the piezoelectric strain coefficient  $d_{33}$  of ceramics can be significantly improved by texturing along preferred crystallographic direction through templated grain growth (TGG) method [14,15]. For example, <001> textured PMN-PT and PMN-PZT piezoelectric ceramics with a texture degree >90% can exhibit a high  $d_{33}$  of 1000 pC N<sup>-1</sup>, which is about two times higher than that of the randomly oriented grain ceramics [16,17]. The enhanced  $d_{33}$  of textured ceramic is attributed to the strong piezoelectric anisotropy and engineered domain states similar to that of single crystal. However, the  $Q_{\rm m}$  value of <001> textured PMN-PT and PMN-PZT is quite low, as shown in Fig. 1b. Hard textured ceramics with moderate values of  $d_{33}$  and  $Q_{\rm m}$  have been developed by integrating TGG process and acceptor doping, but these values were not sufficient to meet the application requirements.

Here we developed a high-power textured piezoelectric ceramic that simultaneously exhibits high  $d_{33}$ ,  $Q_{\rm m}$  and  $E_{\rm c}$  through a synergistic design strategy that combines composition/phase selection, crystallographic texturing and defect engineering. We start with base composition of relaxor-based Pb( ${\rm In_{1/2}Nb_{1/2}}$ )O<sub>3</sub>-Pb( ${\rm Mg_{1/3}Nb_{2/3}}$ )O<sub>3</sub>-PbTiO<sub>3</sub> (PIN-PMN-PT) ternary ferroelectrics with a morphotropic phase boundary (MPB) composition of 0.24PIN-0.42PMN-0.34PT, which possesses higher coercive field ( $E_{\rm c}$ ) in comparison with PMN-PT while retaining the comparable piezoelectric properties [18]. The base composition was co-doped with 2 mol.% MnO<sub>2</sub> and 0.25 wt% CuO to improve the  $Q_{\rm m}$  value through defect engineering and sintering through grain growth. Microstructural engineering involved texturing of 2 mol.% MnO<sub>2</sub> and 0.25 wt%

CuO co-doped PIN-PMN-PT ceramics through TGG method. <001> textured and 2 mol.% MnO<sub>2</sub> and 0.25 wt% CuO doped 0.24PIN-0.42PMN-0.34PT are shown to possess excellent combination of soft and hard piezoelectric properties ( $d_{33}=713~\rm pC~N^{-1},~k_{31}=0.52,~Q_m\approx950,~E_c=9.6~\rm kV~cm^{-1},~tan~\delta=0.45\%$ ). Fabricated textured ceramics exhibit significantly improved combination of both  $Q_m$  and  $d_{33}$  in comparison with the state-of-art commercial piezoelectric ceramics exhibiting either high  $Q_m$  or high  $d_{33}$  value but not both at the same time, as shown in Fig. 1a. From Fig. 1b, it can be seen that this newly designed high power textured ceramic exhibits the best high-power properties ( $d_{33}$ ,  $Q_m$  and  $E_c$ ) in comparison with other reported textured ceramics and even single crystal counternant

# 2. Experimental procedure

The composition of MnO $_2$ - and CuO- co-doped 0.24PIN-0.42PMN-0.34PT was 2 mol.% MnO $_2$  and 0.25 wt% CuO-doped 0.24Pb(In $_{1/2}$ Nb $_{1/2}$ )O $_3$ -0.42Pb(Mg $_{1/3}$ Nb $_{2/3}$ )O $_3$ -0.34PbTiO $_3$ . The 0.24PIN-0.42PMN-0.34PT and 2 mol.% MnO $_2$ -doped 0.24PIN-0.42PMN-0.34PT matrix powders were synthesized using two-step columbite precursor method. First, the mixture of In $_2$ O $_3$  (99.9%) and Nb $_2$ O $_5$  (99.9%) powders were sintered at 1100 °C for 7 h to prepare InNbO $_4$  precursor. Then, the raw materials of PbO (99.9%), InNbO $_4$ , MgNb $_2$ O $_6$  (99.9%), TiO $_2$  (99.8%), and MnO $_2$  (99.9%) were mixed in ethanol solvent for 24 h. The mixed powders were dried and calcined at 850 °C for 4 h. Finally, the calcined powders were ball milled again with 1.5 wt% excess PbO in ethanol solvent for 48 h to decrease the particle sizes.

BaTiO<sub>3</sub> (BT) templates were prepared by two-step topochemical microcrystal conversion (TMC) method [23]. Firstly, the Bi<sub>2</sub>O<sub>3</sub> (99.9%) and TiO<sub>2</sub> (99.8%) raw materials were mixed together with salts (NaCl and KCl with a mole ratio of 1) and the mixtures were heated at 1050 °C for 2 h to obtain the Bi<sub>4</sub>Ti<sub>3</sub>O<sub>12</sub> (BiT) precursors. Then, the BiT precursors and excess BaCO<sub>3</sub> were mixed with salts (NaCl and KCl with a mole ratio of 1) and heated at 970 °C for 2 h to synthesize BaTiO<sub>3</sub> platelets. Next, the ceramic slurry was prepared by mixing the 2 mol.% MnO<sub>2</sub>-doped 0.24PIN-0.42PMN-0.34PT matrix powders with polyvinyl butyral (PVB) binder, toluene solvent and 0.25 wt% CuO. x vol.% BT templates (x=0.5, 1, 2) were mixed into the as-prepared ceramic slurry by magnetic stirring. The slurry was casted using a doctor blade with a height of 0.25 mm. Afterwards, the dried green tapes

were cut, stacked, and laminated under a 20 MPa pressure at 80 °C for 15 min to fabricate green samples. The green samples were heated to 550 °C with a heating rate of 0.6 °C/min<sup>-1</sup> to remove the organic binder and then cold-isostatic pressed at 200 MPa for 1 min. Finally, the samples were embedded in calcined 2 mol.% MnO<sub>2</sub>-doped 0.24PIN-0.42PMN-0.34PT powders with 1.5 wt% excess PbO and sintered at 1200-1220 °C for 6 h in air.

The crystal phases and microstructures of the textured samples were determined using X-ray diffraction (XRD, PANalytical Empyrean) and field-emission scanning electron microscopy (FE-SEM Apreo) in combination with electron backscatter diffraction (EBSD), respectively. The degree of pseudo-cubic <001> texture F was determined from the X-ray diffraction patterns by Lotgering factor method [24,25]. To conduct electrical measurements, the sample surfaces were coated with silver paste and then fired at 550 °C for 30 min. All the samples were poled in silicon oil at 140 °C for 30 min under an electric field of 40 kV/cm<sup>-1</sup>. The piezoelectric coefficient ( $d_{33}$ ) was measured by using a quasi-static  $d_{33}$ meter (YE2730A, APC Products). The temperature-dependent dielectric permittivity ( $\varepsilon_r$ ) and loss tangent (tan  $\delta$ ) were measured with a multifrequency LCR meter (HP4284A) at 1 kHz from 25 °C to 250 °C. Polarization vs. electric field (P-E) hysteresis loop and the piezoelectric strain were measured at 1 Hz using Precision Premier II ferroelectric Tester (Radiant Technologies). The mechanical coupling coefficient (k) and mechanical quality factor  $(Q_m)$  were calculated from the impedance spectra by resonance and antiresonance technique using impedance analyzer (Keysight E4990A) with the applied voltage amplitude of 500 mV. The domain microstructure and the interface between the BT template and textured grain were observed by FEI dual aberration corrected Titan<sup>3</sup> G2 60-300 S/TEM at 300 kV. The energy dispersive X-ray spectroscopic (EDS) elemental maps of the sample were collected by using a SuperX EDS system under STEM mode. Cross-sectional TEM samples were prepared using a FEI Helios 660 focused ion beam (FIB) system. A thick protective amorphous carbon layer was deposited over the region of interest. Then, Ga+ ions (30 kV then stepped down to 1 kV to avoid beam damage to the sample surface) were used to make the sample electron transparent. The atomic positions of the STEM images were determined by using two-dimensional Gaussian fitting in Atomap software [26].

The high-power piezoelectric vibration characteristics of textured, random, and commercial "hard" PZT (APC 841) samples were measured in the transverse mode (31-mode) using a laser vibrometer (PSV-500 by Polytec) aligned toward the sample surface in the displacement direction. The schematic diagram of the measured sample geometries is shown in Fig. S11.

### 3. Results and discussion

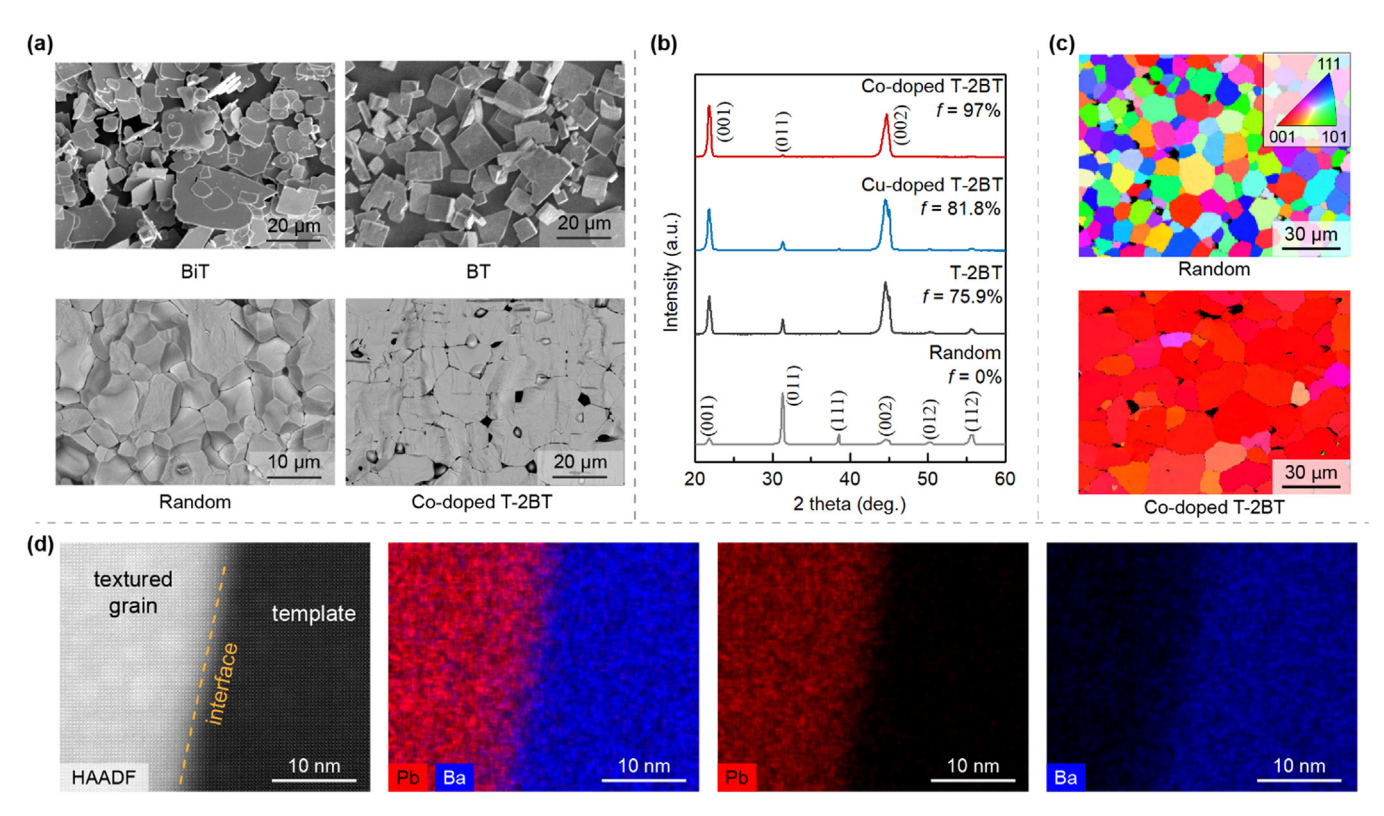
#### 3.1. Fabrication of <001>-textured ceramics

Fig. 2a shows the scanning electron microscopy (SEM) images of the  $\text{Bi}_4\text{Ti}_3\text{O}_{12}$  (BiT) precursors and  $\text{BaTiO}_3$  (BT) templates after the topochemical conversion reaction. The BiT precursors had a plate-like high-aspect ratio with a diameter of  $10\,\mu\text{m}$  and thickness of  $0.2\,\mu\text{m}$ . The final product of the reaction, BT template, maintains the platelet shape inherited from the BiT precursor considering their topotactic relationship. Fig. 2b shows the X-ray diffraction (XRD) patterns for random and <001>-textured ceramics, confirming the formation of perovskite phase. In contrast to the randomly oriented counterpart, the intensities of  $\{00l\}$  peaks are much stronger than other diffraction peaks in the textured sample, indicating strong grain orientation along  $\langle 00l \rangle$  direction. Lotgering factor calculation reveals that the undoped and Cu-doped textured ceramics with 2 vol.% BT templates (abbreviated as T-2BT and Cu-doped T-2BT respectively) can exhibit an orientation/texturing

degree  $F_{001}$  of  $\sim$ 75.9% and 81.8%, respectively, indicating that the CuO addition can enhance the texture development of PIN-PMN-PT ceramics (see Supplementary Note 1). Surprisingly, after MnO<sub>2</sub>-doping, the MnO<sub>2</sub> and CuO co-doped textured ceramics (abbreviated as co-doped T-2BT) can possess even higher texturing degree  $F_{001}$  of ~97%, indicating that the MnO<sub>2</sub> doping can further promote the texture development in CuO-doped PIN-PMN-PT ceramics by facilitating the matrix grain growth around the BT template, as shown in Fig. S1. The enhanced grain growth after MnO<sub>2</sub>-doping has also been observed in PZT-PZN ceramics, which is hypothesized to be driven by diffusion of oxygen vacancies [27]. The increased oxygen vacancies induced by MnO<sub>2</sub>-doping will assist the lattice diffusion resulting in the enhanced grain growth [27]. The electron backscatter diffraction (EBSD) mapping images further confirm the high <001> orientated grains in co-doped T-2BT ceramic compared to random counterpart, as shown in Fig. 2c. Fig. 2a also shows the microstructures for both random and co-doped T-2BT ceramics. The co-doped T-2BT ceramic exhibits well-oriented matrix grains with brick wall-like microstructure, representing the texturing development, in comparison with the random counterpart exhibiting equiaxed grains. Then, the EDS was applied for analyzing the distribution of the different elements across the co-doped T-2BT ceramic. As shown in Fig. S3, the Mn element was homogenously distributed inside the co-doped T-2BT ceramic, indicating that all the Mn substitutes in the lattice. The solubility limit of MnO<sub>2</sub> in the PIN-PMN-PT lattice is reported to be  $\sim$ 2 mol.% [28]. In this study, the addition of 2 mol.% MnO<sub>2</sub> and 0.25 wt% CuO already exceeded the solubility limit of the lattice, leading to the agglomeration of CuO on the grain boundary, as shown in Fig. S3. The reduced solubility of CuO in the lattice will lead to the formation of liquid phase at grain boundary, which will enhance the textured grain growth. In addition, the secondary phases with rich In and Mg elements were found in the co-doped T-2BT ceramic. This result indicates that the Mn ions substitute into the B-site of the ABO3 structure and contributes to the formation of secondary phases. Fig. 2d shows the high-magnification EDS element mapping of an interface between BT template and textured grain. The interface between the <001> BT template and matrix grain is quite sharp, indicating that the BT template is stable inside the matrix grain.

# 3.2. Enhanced soft and hard piezoelectric properties

Fig. 3a shows the dielectric permittivity as a function of temperature for both random and textured ceramics. The co-doped T-2BT ceramic can exhibit a relatively high Curie temperature  $(T_c)$ around 205 °C in comparison with the random counterpart with a  $T_{\rm c}\sim 216$  °C, indicating that the low concentration of BT template inside the textured ceramics has little influence on its Curie temperature. Fig. 3b shows the P-E hysteresis loops for random, textured ceramics and single crystal counterpart. Both random and textured ceramics exhibit well-saturated P-E hysteresis loop along with high remanent polarization  $(P_r)$  and high coercive field  $(E_c)$ . The coercive field  $E_c$  for co-doped T-2BT ceramic is 9.7 kV cm<sup>-1</sup>, which is higher than that of the T-2BT ceramic  $\sim$ 9.1 kV cm<sup>-1</sup>, indicating the higher stability of co-doped T-2BT ceramic under high electric fields. In addition, compared to the random counterpart, the Cu-doped T-2BT ceramic possesses lower  $P_r$  and higher  $E_c$ . The lower  $P_r$  value can be attributed to the composite effect of BT template since BT template has low  $P_{\rm r}$  value of 12  $\mu$ C cm<sup>-2</sup> [29]. The higher  $E_c$  can be explained by the increased tetragonality degree of textured ceramic, as shown in Fig. S5. In contrast to the common belief that the Pr of MnO2-doped ceramic is always lower than that of undoped counterpart due to the hardening effect of  $MnO_2$ -doping, the co-doped T-2BT ceramic possesses higher  $P_r$  in comparison with T-2BT ceramic, as shown in Fig. 3b. The lower  $P_r$ 



**Fig. 2. Microstructures and texture quality of ceramics.** (a) SEM images of Bi<sub>4</sub>Ti<sub>3</sub>O<sub>12</sub> (BiT), BaTiO<sub>3</sub> (BT), PIN-PMN-PT with 0 vol.% BT (abbreviated as random), and 2 mol.% MnO<sub>2</sub> and 0.25 wt% CuO co-doped PIN-PMN-PT with 2 vol.% BT (abbreviated as co-doped T-2BT) ceramics. (b) XRD patterns of PIN-PMN-PT with 0 vol.% BT (random), PIN-PMN-PT with 2 vol.% BT (abbreviated as T-2BT), 0.25 wt% CuO-doped PIN-PMN-PT with 2 vol.% BT (Cu-doped T-2BT), and 2 mol.% MnO<sub>2</sub> and 0.25 wt% CuO-doped PIN-PMN-PT with 2 vol.% BT (co-doped T-2BT) ceramics. (c) EBSD images of random and co-doped T-2BT ceramics. (d) STEM image and the corresponding EDS element mapping of co-doped T-2BT ceramic.

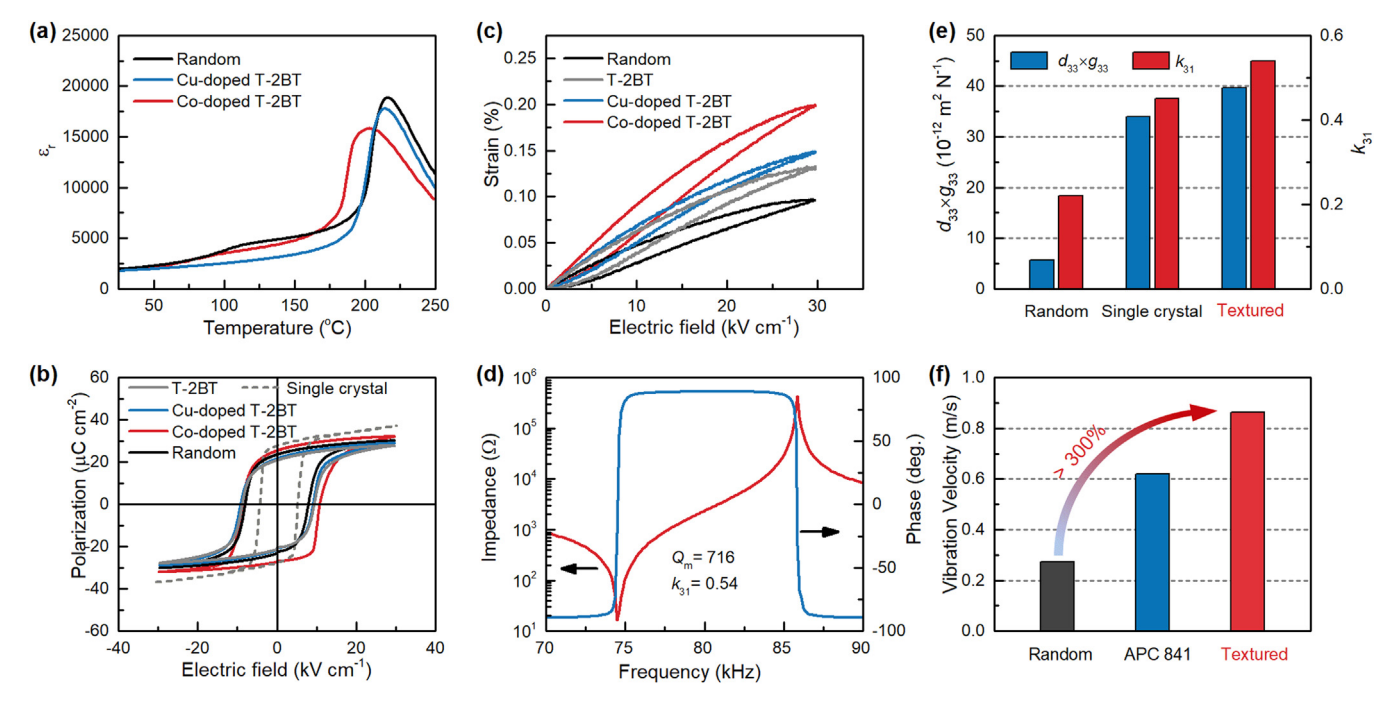


**Fig. 3. Dielectric and piezoelectric properties.** (a) Dielectric permittivity for random, Cu-doped T-2BT, and co-doped T-2BT ceramics, measured at 1 kHz; (b) P-E hysteresis loops for random, T-2BT, Cu-doped T-2BT, and co-doped T-2BT ceramics, measured at 1 Hz. The P-E loop for MnO<sub>2</sub> doped PIN-PMN-PT single crystal is from Ref. [11] (c) Unipolar S-E curves for random, T-2BT, Cu-doped T-2BT, and co-doped T-2BT ceramics, measured at 1 Hz. (d) Impedance and phase angle spectra for co-doped T-2BT ceramic, measured with the applied voltage amplitude of 500 mV. (e) Comparison of piezoelectric figure of merit  $d_{33} \times g_{33}$  and  $k_{31}$  for random, MnO<sub>2</sub> doped PIN-PMN-PT single crystal and co-doped T-2BT ceramics [11]. (f) Comparison of maximum vibration velocities for random, APC 841, and co-doped T-1BT ceramics ( $k_{31}$  mode).

**Table 1**Dielectric and piezoelectric properties for both random and textured piezoelectric ceramics.

Specimen	Template	$F_{001}$ (%)	$T_{\rm c}$	$E_{\rm c}$ (kV cm <sup>-1</sup> )	$\varepsilon_{33}^{\mathrm{T}}/\varepsilon_{\mathrm{o}}$	tan $\delta$ (%)	$d_{33} \; ({ m pC} \; { m N}^{-1})$	$g_{33}~(\times~10^{-3}~V~m~N^{-1})$	$d_{31} \; ({ m pC} \; { m N}^{-1})$	$k_{31}$	$Q_{\rm m}$
Co-doped T-2BT	2 vol.% BT	97	205	9.7	1498	0.42	725	54.7	247	0.54	716
Co-doped T-1BT	1 vol.% BT	94.2	205	9.6	1588	0.45	713	50.7	240	0.52	949
Co-doped T-0.5BT	0.5 vol.% BT	64	205	9.9	1483	0.45	465	35.4	157	0.40	1542
Cu-doped T-2BT	2 vol.% BT	81.8	214	9.15	1786	1.05	410	25.9	138	0.29	149
T-2BT	2 vol.% BT	75.9	216	9.1	1310	1.18	364	31.4	117	0.28	120
Random	0	0	216	8.0	1836	0.96	304	18.7	101	0.22	147
Commercial APC 841	0	0	273	-	1152	0.50	312	29.9	108	0.33	1050

of T-2BT ceramic can be understood from its impedance spectra shown in Fig. S6. It is known that the maximum impedance phase angle  $\theta_{\rm Z}$  in resonance and anti-resonance regions can be used to judge the poling degree of piezoelectric ceramics [30]. The low  $\theta_{\rm Z}$ of 64.1° indicates a low poling degree of T-2BT ceramic, resulting in lower  $P_r$ . Fig. 3c shows the strain response under electric field for both textured and random ceramics. The textured ceramics exhibit over 2 times improvement in strain value at the same electric field in comparison with random counterpart. Fig. 3e shows the piezoelectric figure of merit  $d_{33} \times g_{33}$  and electromechanical coupling factor  $k_{31}$  for random, textured ceramics and single crystal counterpart. The textured ceramic exhibits a large  $d_{33} \times g_{33}$  value of  $39.7 \times 10^{-12}$  m<sup>2</sup> N<sup>-1</sup>, due to high  $g_{33}$  value of  $54.7 \times 10^{-3}$  V m  $N^{-1}$ , which is the result of the significantly improved  $d_{33}$  and suppressed dielectric permittivity. Besides, in contrast to both random and single crystal counterparts, the textured ceramic can possess higher  $k_{31}$  value of 0.54. Electromechanical properties such as Q<sub>m</sub> are obtained from the electrical impedance method based on IEEE standard (Fig. 3d). Detailed dielectric and piezoelectric properties of both random and textured ceramics are summarized in Table 1. The combination of high  $d_{33} \sim 725$  pC N<sup>-1</sup> and Q<sub>m</sub>  $\sim 716$ along with high  $k_{31}$  of 0.54 is obtained in co-doped T-2BT sample with a 97% texturing degree. Notably, the co-doped T-1BT ceramics also show an excellent combination of soft and hard piezoelectric properties ( $d_{33} = 713 \text{ pC N}^{-1}$ ,  $k_{31} = 0.52$ ,  $Q_m \approx 950$ ), which is significantly better than those of the random, Cu-doped T-2BT and commercial "hard" PZT ceramics (APC 841), as shown in Table 1. Then, the high-power piezoelectric vibration characteristics of textured ceramic were investigated and compared with that of the random counterpart and APC 841 ceramic (Fig. S11). Fig. 3f shows the maximum vibration velocities for random, APC 841, and textured ceramics ( $k_{31}$  mode). The textured ceramic exhibits a vibration velocity of 0.86 m s<sup>-1</sup>, which is over 300% higher than that of the random counterpart. The vibration velocity of textured ceramic is also higher than that of the APC 841 ceramic  $\sim 0.62$  m s<sup>-1</sup>, demonstrating that textured ceramics are good candidates for high-power piezoelectric device applications.

# 3.3. Origin of enhanced piezoelectric properties

As shown in Table 1, the  $d_{33}$  of co-doped T-2BT sample is much higher than that of T-2BT sample, which is attributed to the improved <001> texturing degree ( $F_{00l}$  value from 75.9% to 97%) and poling degree ( $\theta_Z$  value from 64.1° to 89.1°) induced by MnO<sub>2</sub>doping effect. The transmission electron microscopy (TEM) imaging of ferroelectric domain structure within the textured grain of co-doped T-2BT sample is shown in Fig. 4a. A large fraction of stripe-type nanodomains can be observed and they are parallel to each other. The nanodomain with size of 15-20 nm can be observed (see the inset of Fig. 4a). According to previous studies, the appearance of nanodomains microstructure might be thermodynamically driven by the reduced domain wall energy near MPB region since the domain size D has been reported to be proportional to the square root of domain wall energy (D  $\propto \sqrt{\gamma}$ ) [31,32]. An atomic-resolution STEM image of the interface between the BT template and PIN-PMN-PT grain in co-doped T-2BT sample is

shown in Fig. 4b. A defect-free coherent interface can be observed, proving the excellent lattice match between the BT template and matrix grain. The defect-free interface is important for achieving enhanced piezoelectric response since the defects at the interface can act as the pinning center to restrict the movement of ferroelectric domain walls. The FFT patterns extracted from the textured grain and BT template clearly show <001>c orientation of both textured grain and BT template. In contrast to classical ferroelectrics, relaxor-PT systems, such as PMN-PT, possess a unique characteristic, that is, the nanoscale structural heterogeneous regions or so-called polar nanoregions (PNRs) [33,34], which are responsible for the high piezoelectricity in relaxors [33,35]. Recently, STEM has been utilized to identify the presence of nanoscale structural heterogeneous regions in relaxor-PT systems and the size of nanoscale domains was found to vary from 2 to 12 nm [36,37]. In our work, similar approach has been applied. The magnified STEM image of the atomic columns inside the textured grains is shown in Fig. 4c. The red and blue circles denote the A-site and B-site cations, respectively. Owing to the weak scattering factor of the electrons, the  $O^{2-}$  columns are hard to be visualized [38]. The polar vectors for one unit-cell column can be represented as the atomic displacements from the center of the B-site cation to the center of the nearest neighboring A-site cations [37]. As shown in Fig. 4c, given that the co-doped T-2BT sample has a rhombohedral phase structure (Fig. S5), the polar vector along the rhombohedral <111> direction (marked by a large rectangular box in Fig. 4c) can be observed. Besides, the tetragonal region with polar vector along <001> direction can be found as well, indicating the coexistence of phases and confirming the vicinity to MPB. Nanoscale structural heterogeneity (the coexistence of rhombohedral and tetragonal nanoregions) with the size comparable to previous reports is observed within the textured matrix grain. This assists in increasing the interfacial energy and minimizing the polarization discontinuity, which leads to flattened free-energy curve and enhancement of piezoelectricity [37].

To better understand the high piezoelectric properties of textured ceramics, the orientation dependence of piezoelectric response was calculated using phase structural relationships. For the ferroelectric crystals in rhombohedral 3m group, using spherical coordinates, the orientation dependence of longitudinal  $d_{33}$  piezoelectric coefficient can be represented as [39]:

$$d_{33}^{r^*}(\theta, \phi) = d_{15}^r \cos\theta \sin^2\theta - d_{22}^r \sin^3\theta \cos 3\phi + d_{31}^r \sin^2\theta \cos\theta + d_{33}^r \cos^3\theta$$
 (1)

The parameters obtained from the rhombohedral PIN-PMN-PT single crystal were used to plot the 3D surface of  $d_{33}^*$  [40]. The orientation dependence of piezoelectric coefficient is shown in Fig. S15a. It is obvious that  $d_{33}$  is strongly dependent on the crystallographic orientation and the maximum  $d_{33}$  along the [001] nonpolar direction is over 10 times higher than that along [111] polar direction. Thus,  $d_{33}$  can be enhanced significantly along [001] nonpolar direction due to the strong piezoelectric anisotropy of rhombohedral PIN-PMN-PT.

To express the piezoelectric anisotropy theoretically for <001>-textured ceramics, a parameter  $D_{int}$  is defined as

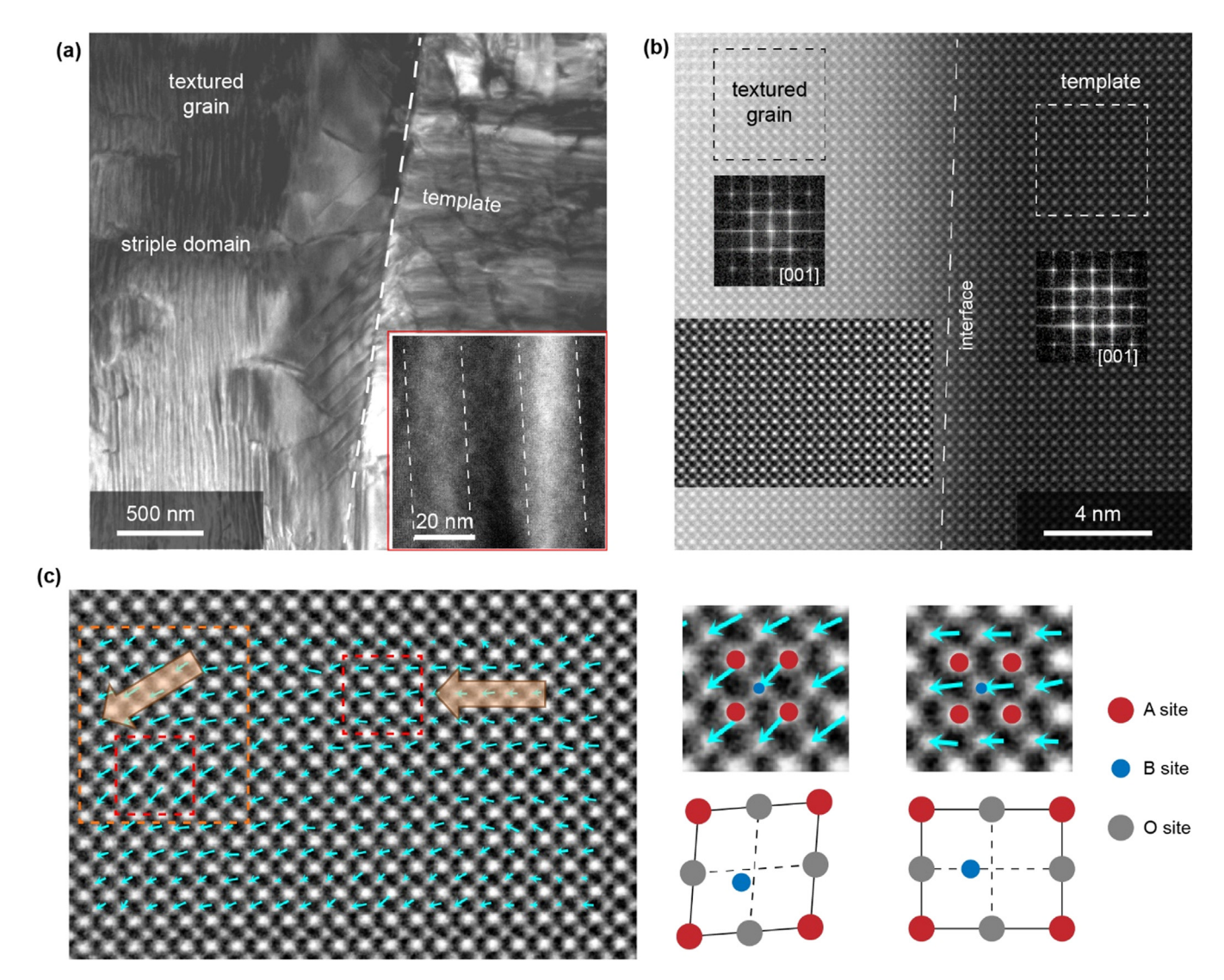


**Fig. 4. Microstructures of co-doped T-2BT.** (a) High-magnification bright field TEM images of ferroelectric domains for co-doped T-2BT ceramic and the inset shows nanodomains within the textured grain. (b) Atomic-resolution HAADF-STEM image of the interface between BT template and textured grain with the inset showing the corresponding faster Fourier transform (FFT) patterns. (c) Atomic-resolution STEM image of the region inside the textured grain along <001>, with B-site cation displacement vectors (arrows) map. The enlarged images on the right show the positions for A and B-site atomic columns.

 $D_{
m int}=d_{33
m int}^{tex}/d_{33
m int}^{ran}$ , where  $d_{33
m int}^{tex}$  and  $d_{33
m int}^{ran}$  represent the intrinsic piezoelectric coefficient of textured and random ceramics, respectively. The explanations for the intrinsic piezoelectric coefficient of textured and random ceramics can be found in Supplementary Note 3. Previous reports have shown that the calculated  $D_{
m int}$  value for rhombohedral phase is about 2.2 [2,41], theoretically proving that the piezoelectric response of <001>-textured ceramic is higher than that of random ceramic. Experimentally observed piezoelectric anisotropy for textured ceramic can be expressed using the parameter  $D_{exp}=d_{33exp}^{tex}/d_{33exp}^{ran}$ , where  $d_{33exp}^{tex}$  and  $d_{33exp}^{ran}$  represent the measured piezoelectric coefficient of textured and random ceramics, respectively. The calculated  $D_{exp}$  value of textured ceramic is 2.4, which is consistent with its theoretical calculated value.

#### 3.4. Understanding of the improved mechanical quality factor

As shown in Table 1, textured ceramics can exhibit high mechanical quality factor  $Q_{\rm m}$  values. For MnO<sub>2</sub>-doped rhombohedral ferroelectrics, their spontaneous polarization  $P_{\rm S}$  is along the <111> direction (Fig. S16a). Acceptor ions like Mn<sup>2+</sup> or Mn<sup>3+</sup> will substi-

tute center B-site of perovskite structure due to the similar ionic radius, creating defect dipole consisting of negatively charged acceptor ions and positively charged oxygen vacancies. The defect dipole will then generate a defect polarization  $P_{\rm D}$  along the same direction <111> of spontaneous polarization  $P_{\rm S}$  based on symmetry conforming assumptions (Fig. S16c). The explanations for symmetry conforming assumptions can be found in Supplementary Note 5. After the application of the external electric field E, as shown in Fig. S16f, the  $P_{\rm S}$  will switch to the same direction of E, while the defect dipoles and related polarization  $P_{\rm D}$  are hard to be switched since the reorientation of defect dipoles requires the oxygen vacancy  $V_{\rm O}$  diffusion, and polarization switching under electric field is a diffusionless process [42]. In addition, according to previous reports, the relaxation time of  $P_{\rm D}$  (10<sup>5</sup> s) is much longer than that of  $P_{\rm S}$ , which is in the range of  $10^{-6}$  to  $10^{-5}$  s [43].

The dynamics of  $P_D$  under external electric field E can be estimated by analyzing the evolution of internal bias field  $E_i$  as a function of electric field. The horizontal shift of P-E hysteresis loops can be observed in MnO<sub>2</sub>-doped ceramics in comparison with undoped counterpart as shown in Fig. 3b, indicating the existence of internal bias field  $E_i$ . The  $E_i$  value can be calculated by using the

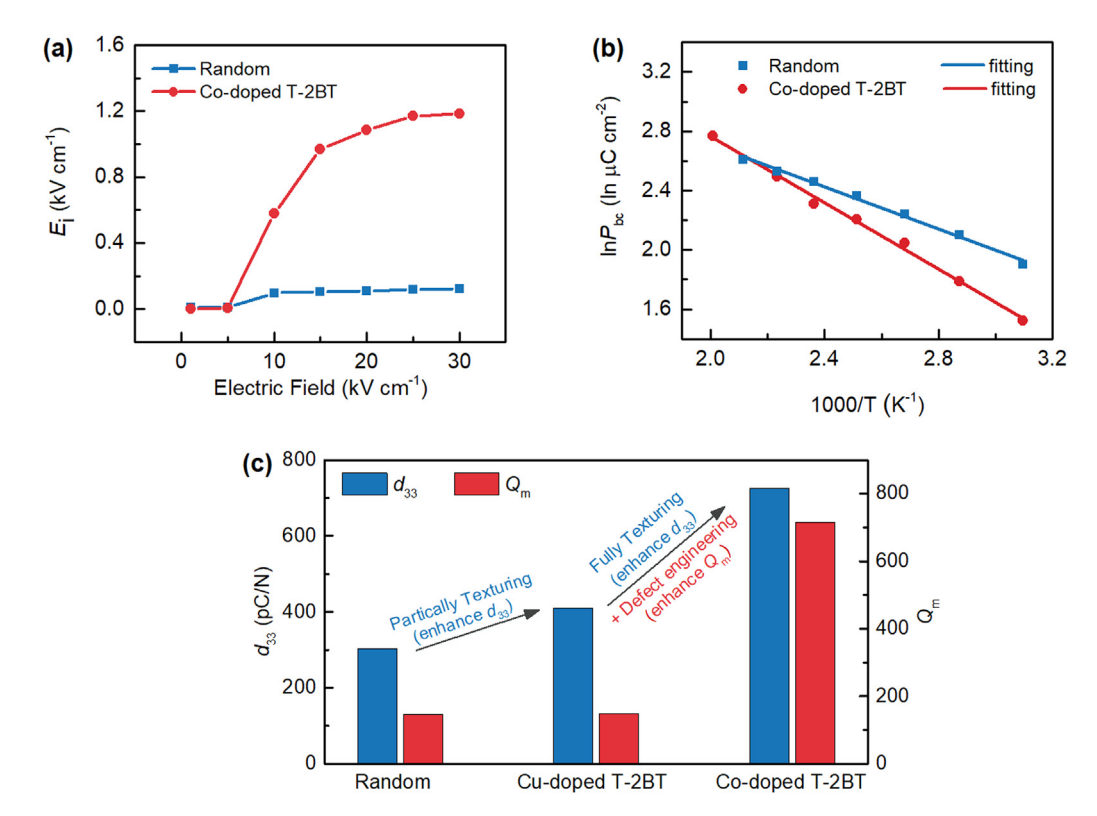


Fig. 5. Comparison of polarization switching and high-power piezoelectric properties for random and co-doped textured ceramics. (a)  $E_i$  as a function of the poling E field for random and textured ceramics. (b) Plot of  $\ln(P_{\rm bc})$  versus inverse temperature for random and textured ceramics. (c) Comparison of piezoelectric properties of random, Cu-doped T-2BT, and co-doped T-2BT ceramics in terms of  $d_{33}$  and  $Q_{\rm m}$ .

equation,  $E_{\rm i}=(E_{\rm c^+}+E_{\rm c^-})/2$ , where  $E_{\rm c^+}$  and  $E_{\rm c^-}$  are the coercive field values of forward and backward polarization switching process, respectively [44]. The large  $E_{\rm i}$  value of MnO<sub>2</sub>-doped ceramics suggests that the defect polarization  $P_{\rm D}$  restricts polarization switching in the opposite direction. In addition, as shown in Fig. 5a, the internal bias field  $E_{\rm i}$  is directly proportional to the poling electric field  $E_{\rm i}$ . Specifically,  $E_{\rm i}$  increases dramatically as the poling electric field  $E_{\rm i}$  increases to 15 kV cm<sup>-1</sup> and then saturates with further increase in the  $E_{\rm i}$  to 30 kV cm<sup>-1</sup> for textured sample, while the  $E_{\rm i}$  value for random sample is pretty small and remains nearly constant with increasing electric field. These results confirm that  $E_{\rm i}$  originates from the motion of defect dipole under electric field.

The dynamics of polarization switching under electric field can be analyzed by calculating the activation energy  $E_{\rm a}$  for polarization switching. The activation energy is determined to be 0.1 eV for textured sample, which is much higher than that of random sample (0.06 eV) as shown in Fig. 5b, experimentally demonstrating that the defect dipoles or  $P_{\rm D}$  will restrict the  $P_{\rm S}$  switching in MnO<sub>2</sub>-doped samples. The detailed explanation on activation energy can be found in Supplementary Note 6.

Based on these discussions, when an external electric field E is applied to the sample, the spontaneous polarization  $P_{\rm S}$  will prefer to switch in the same direction as that of E, while the defect dipole induced polarization  $P_{\rm D}$  is hard to be switched under electric field E and maintains its original direction, generating a restoring force to restrict the polarization switching under electric field. It is known that the polarization switching under external electric field makes a huge contribution to the mechanical loss in ferroelectrics; mechanical loss is the inverse of mechanical quality factor  $Q_{\rm m}$  [44,45]. Thus, the restricted polarization switching/rotation induced by the existence of defect dipoles or  $P_{\rm D}$  will result in reduced mechanical loss and improved mechanical quality factor  $Q_{\rm m}$  value in acceptor-doped ferroelectrics.

The <001> textured  $MnO_2$ - and CuO-doped PIN-PMN-PT ceramics can possess both enhanced soft and hard piezoelectric properties in comparison with random ceramics (Fig. 5c), where the enhanced soft piezoelectric response originates from the strong anisotropy and increased intrinsic piezoelectric response in textured ceramics. The enhanced hard piezoelectric response stems from the restricted polarization switching induced by the unswitchable defect dipoles or  $P_D$ .

# 3.5. Phase-field simulations

To gain insight into how the presence of defect dipoles can influence the P-E loops and the domain wall motion, we performed phase-field simulations [46] to model the domain structure evolution under an alternating electric field for the undoped and co-doped textured piezoceramics, from which the P-E loops can be obtained. Considering the highly [001]-textured nature of the piezoceramics in the experiment, we model the system as a [001]oriented bulk single crystal and assume the initial domain configuration to be layered structure consisting of two domain variants,  $P_{\rm s} \parallel [11\bar{1}]$  or  $[\bar{1}\bar{1}\bar{1}]$  which are separated by horizontal 109° domain walls. The domain periodicity of the initial state is assumed to be  $\sim$  20 nm, as informed from the HAADF STEM image of Fig. 4a. For simplicity, we adopt the model parameters of rhombohedral PMN-30PT developed in ref. [47] to represent the case for 0.24PIN-0.42PMN-0.34PT. Since both materials are relaxor-based ferroelectric materials and share the same rhombohedral R3m symmetry as the ground state, we expect that the results obtained here can be applied to the case for 0.24PIN-0.42PMN-0.34PT. The doping effect by MnO2 and CuO is considered by introducing a set of randomly distributed defect dipoles with defect polarization  $|P_D| = 0.024$  C  $\mathrm{m}^{-2}$  and a concentration ( $x_D = 3\%$ ) based on an approach similar to that in ref. [48]. Each local defect polarization is assumed to be

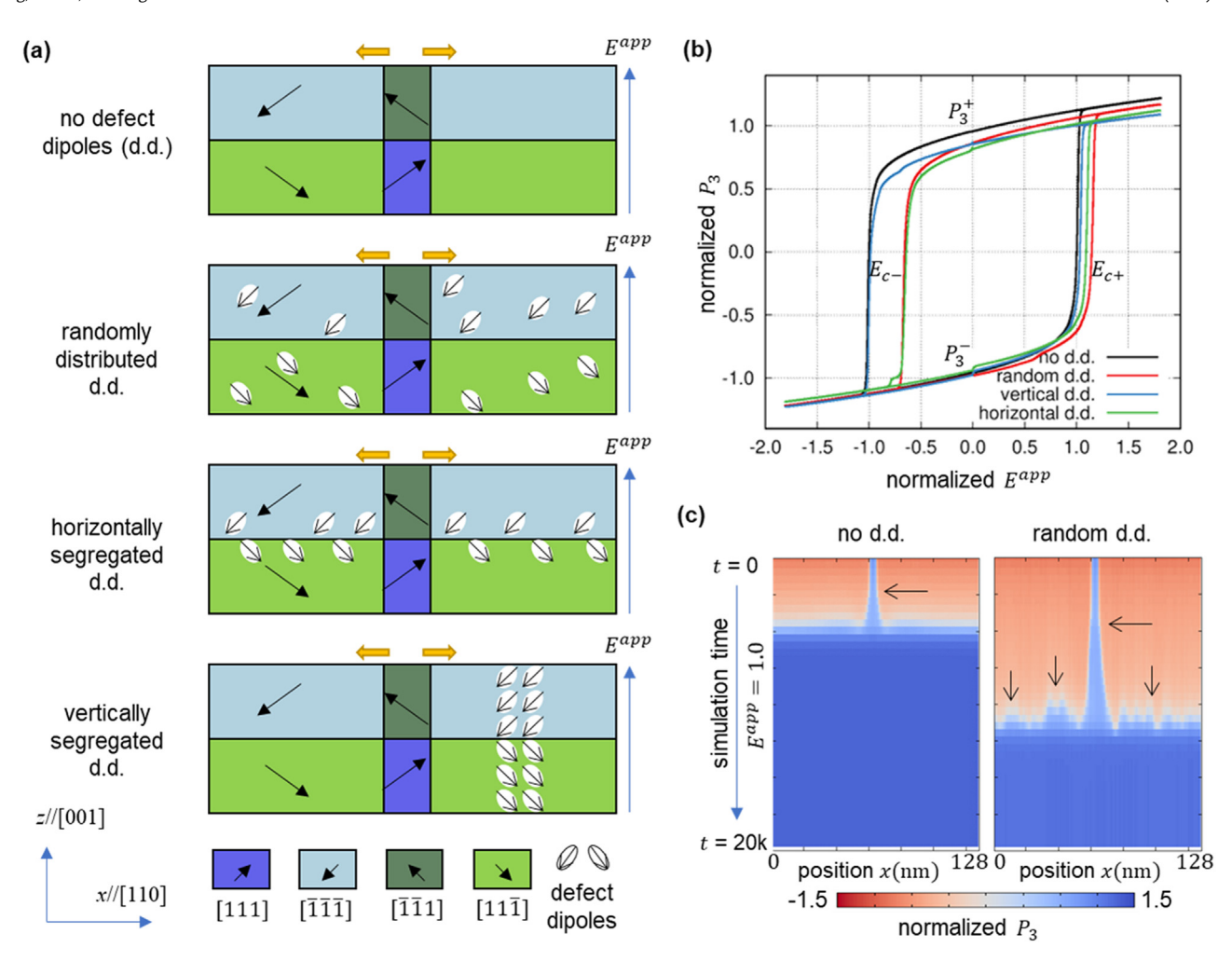


Fig. 6. Phase-field modeling of the influence of the presence and spatial distribution of defect dipoles on the *P-E* loops. (a) Schematics of the model systems with layered domain structures consisting of rhombohedral domain variants separated by (001)-oriented 109° domain walls without and with defect dipoles. In the doped system, the defect dipoles are considered to be randomly distributed within the entire system or segregated horizontally/vertically along the horizontal/vertical domain walls. The concentration is controlled to be ~3.0%. A pair of nuclei of the reversed domain variants (dark blue and dark green colors) is introduced to enable the switching to occur via sideway domain wall motion (as labelled by the yellow arrows). (b) The corresponding *P-E* loops for each case in (a). The polarization  $P_3$  is normalized with respect to  $P_5$  and the applied electric  $E_3^{app}$  is normalized with respect to  $P_5$  of the undoped case. (c) The 1D spatial distribution of normalized  $P_3$  (averaged over all  $P_3$  grid points for each grid point  $P_3$ ) as a function of the simulation time under a constant applied electric  $P_3^{app} = P_5$ , showing the motion of domain wall during switching and the pinning effect by defect dipoles for the randomly distributed case. The horizontal arrows label the onset of domain wall motion. The vertical arrows label the rugged front of domain switching due to the presence of local defect dipoles.

aligned with the ferroelectric polarization of the surrounding domain variants of the <001>-poled state, i.e.,  $P_D \parallel [11\bar{1}]$  or  $[\bar{1}\bar{1}]$ . To study the pinning effect of defect dipoles on domain wall motion, a pair of nuclei of reversed ferroelectric polarization is introduced, i.e.,  $P_S \parallel [111]$  or  $[\bar{1}\bar{1}]$ , which creates vertical (110)-oriented domain walls, as shown in Fig. 6a. Upon the application of a reversed electric field, the polarization switching can occur via the sideway propagation of the vertical domain walls (labeled by the yellow arrows). A detailed description of the model setup is given in Supplementary Note 7.

From the calculated *P-E* loops (Fig. 6b), we can see a horizontal shift of the loops toward the right-hand side for the doped system with randomly distributed defect dipoles compared with the undoped case, suggesting the presence of an internal bias field  $E_{\rm i}$  as seen in the experiments. Particularly, the coercive field  $E_{\rm c+}$  increases slightly by  $\sim 20\%$ , which qualitatively agrees with experiments (Fig. 3b) for both cases, while  $E_{\rm c-}$  decreases more significantly by  $\sim 40\%$ , which results in a reduction of the averaged coercive field  $E_{\rm c} = (|E_{\rm c+}| + |E_{\rm c-}|)/2$  and is different from experiments. To understand why this discrepancy happens, we performed further simulations by considering different spatial distributions of

the defect dipoles, namely, the horizontal segregation and vertical segregation, which corresponds to accumulation of defect dipoles in the proximity of horizontal or vertical domain walls, respectively. The calculated P-E loop for the horizontally segregated case shows similar behavior as the randomly distributed one but the loop for the vertically segregated defect dipoles has negligibly changed  $E_{\text{c-}}$  and  $E_{\text{c+}}$ . Our simulation results suggest that the spatial distribution of defect dipoles can influence the P-E loops and serve as a possible explanation for the hardening effect in co-doped ceramics. It should be noted that many factors not considered here may as well influence the P-E loops for doped ferroelectric ceramics, e.g., grain size, grain boundaries, and defect-induced local strains and associated changes in the energy landscapes, which requires further systematical studies.

To reveal the relationship between the increase in  $E_{\rm c+}$  and the pinning effect of defect dipoles on the domain wall motion, we track the averaged position of the vertical domain walls as a function of simulation time for the undoped case and the doped case with randomly distributed defect dipoles under an identical constant applied electric field, as plotted in Fig.6c. In the presence of defect dipoles, the onset of the sideway domain wall motion

is delayed (indicated by the horizontal black arrows), suggesting a slower switching kinetics. Moreover, there is roughness in the front of the domain switching (indicated by the vertical black arrows) due to the local heterogeneous electric field associated with the defect dipoles, which further suppresses the propagation of the domain walls and postpones overall polarization reversal process. Therefore, the pinning effect of defect dipoles on the domain wall motion may account for the increase in  $E_{\text{C+}}$  of the macroscopic P-E loops for the cases with defect dipoles.

#### 4. Conclusion

In summary, this study successfully addresses grand challenge in fabricating high-performance high-power piezoelectric ceramics through a synergistic design strategy that combines composition/phase selection, crystallographic texturing and defect engineering. Specifically, the fabricated <001> textured MnO2- and CuO-doped PIN-PMN-PT ceramics with 1 vol.% BT templates exhibit ultrahigh combined soft and hard piezoelectric properties  $(d_{33} = 713 \text{ pC N}^{-1}, k_{31} = 0.52, Q_m \approx 950, E_c = 9.6 \text{ kV cm}^{-1}, \text{ tan}$  $\delta = 0.45\%$ ) in comparison with both the state-of-art commercial and reported textured piezoelectric ceramics, which makes the fabricated high-power textured ceramics an outstanding candidate for high-power device applications. A comparative study between the random and <001> textured ceramics indicates that the strong piezoelectric anisotropy, enhanced intrinsic piezoelectric response, and existence of local structure heterogeneity, together contribute towards the greatly improved piezoelectric properties of <001> textured ceramics in comparison with random counterpart. In addition, the restricted polarization switching induced by the unswitchable defect dipoles or PD plays an important role in reducing the mechanical loss  $Q_{\rm m}^{-1}$  and thus improving the mechanical quality factor Q<sub>m</sub> of MnO<sub>2</sub>-doped piezoelectric ceramics in comparison with undoped counterpart. A combination of experiments and phase-field simulations both experimentally and theoretically confirms the restricted P<sub>S</sub> switching in MnO<sub>2</sub>-doped PIN-PMN-PT ceramics. We believe this synergistic design strategy will have tremendous impact in development of new generation of high-power piezoelectric devices.

# **Declaration of Competing Interest**

The authors declare that they have no known competing financial interests or personal relationships that could have appeared to influence the work reported in this paper.

## Acknowledgements

H.L. and Y.Y. acknowledge the financial support from DARPA through award number HR00111920001. H. Liu acknowledges the financial support from National Science Foundation through CREST CREAM program at Norfolk State University. T.Y. and L.-Q.C. are supported as part of the Computational Materials Sciences Program funded by the U.S. Department of Energy, Office of Science, Basic Energy Sciences, under Award No. DE-SC0020145. B.W. acknowledges support by the National Science Foundation (NSF) through Grant No. DMR-1744213. X.L. acknowledges the financial support from Army Research Office through TE3 program (W911NF1620010). S.P. acknowledges the financial support from National Science Foundation through the award number 1936432. The computer simulations were performed using the commercial software package  $\mu$ -PRO (http://mupro.co/contact/) on the ICS-ACI Computing Systems at Pennsylvania State University and at the Extreme Science and Engineering Discovery Environment cluster, which used the Comet system at the UC San Diego. We thank Haiying Wang for TEM sample preparation by using FIB. All microscopy work was performed at Penn State Materials Characterization Laboratory. The authors thank Dr. Harold Robinson, ONR Transduction Materials Project Manager, for constructive discussions of the results that has helped us in improving the quality of presentation.

# Supplementary materials

Supplementary material associated with this article can be found, in the online version, at doi:10.1016/j.actamat.2022.118015.

#### References

- [1] M. Slabki, J. Wu, M. Weber, P. Breckner, D. Isaia, K. Nakamura, J. Koruza, Anisotropy of the high-power piezoelectric properties of Pb(Zr,Ti)O<sub>3</sub>, J. Am. Ceram. Soc. 102 (2019) 6008–6017, doi:10.1111/jace.16464.
- [2] P. Li, J. Zhai, B. Shen, S. Zhang, X. Li, F. Zhu, X. Zhang, Ultrahigh piezoelectric properties in textured (K,Na)NbO<sub>3</sub>-Based lead-free ceramics, Adv. Mater. 30 (2018) 1–9, doi:10.1002/adma.201705171.
- [3] C.W. Ahn, H.C. Song, S. Nahm, S. Priya, S.H. Park, K. Uchino, H.G. Lee, H.J. Lee, Effect of ZnO and CuO on the sintering temperature and piezoelectric properties of a hard piezoelectric ceramic, J. Am. Ceram. Soc. 89 (2006) 921–925, doi:10.1111/j.1551-2916.2005.00823.x.
- [4] S.Y. Yoo, J.Y. Ha, S.J. Yoon, J.W. Choi, High-power properties of piezoelectric hard materials sintered at low temperature for multilayer ceramic actuators, J. Eur. Ceram. Soc. 33 (2013) 1769–1778, doi:10.1016/j.jeurceramsoc.2013.02.014.
- [5] Y. Yan, K.H. Cho, S. Priya, Piezoelectric properties and temperature stability of Mn-doped Pb(Mg<sub>1/3</sub>Nb<sub>2/3</sub>)-PbZrO<sub>3</sub>-PbTiO<sub>3</sub> textured ceramics, Appl. Phys. Lett. (2012), doi:10.1063/1.3698157.
- [6] K. Uchino, Introduction to Piezoelectric Actuators and Transducers, Int. Cent. Actuators Transducers, Pennsylvania State Univ., 2003.
- [7] Z. Li, H.C. Thong, Y.F. Zhang, Z. Xu, Z. Zhou, Y.X. Liu, Y.Y.S. Cheng, S.H. Wang, C. Zhao, F. Chen, K. Bi, B. Han, K. Wang, Defect engineering in lead zirconate titanate ferroelectric ceramic for enhanced electromechanical transducer efficiency, Adv. Funct. Mater. 31 (2021) 1–10, doi:10.1002/adfm.202005012.
- [8] Y. Yan, K.H. Cho, S. Priya, Role of secondary phase in high power piezoelectric PMN-PZT ceramics, J. Am. Ceram. Soc. 94 (2011) 4138–4141, doi:10.1111/j. 1551-2916.2011.04891.x.
- [9] E. Sun, R. Zhang, F. Wu, B. Yang, W. Cao, Influence of manganese doping to the full tensor properties of 0.24Pb(In<sub>1/2</sub>Nb<sub>1/2</sub>)O<sub>3</sub>-0.47Pb(Mg<sub>1/3</sub>Nb<sub>2/3</sub>)O<sub>3</sub>-0.29PbTiO<sub>3</sub> single crystals, J. Appl. Phys. 113 (2013) 1-4, doi:10.1063/1. 4792600
- [10] G. Du, R. Liang, L. Wang, K. Li, W. Zhang, G. Wang, X. Dong, Linear temperature scaling of ferroelectric hysteresis in Mn-doped Pb(Mn<sub>1/3</sub>Sb<sub>2/3</sub>)O<sub>3</sub>-Pb(Zr,Ti)O<sub>3</sub> ceramic with internal bias field, Appl. Phys. Lett. 102 (2013), doi:10.1063/1.
- [11] L. Zheng, R. Sahul, S. Zhang, W. Jiang, S. Li, W. Cao, Orientation dependence of piezoelectric properties and mechanical quality factors of 0.27Pb(In<sub>1/2</sub>Nb<sub>1/2</sub>)O<sub>3</sub>-0.46Pb(Mg<sub>1/3</sub>Nb<sub>2/3</sub>)O<sub>3</sub>-0.27PbTiO<sub>3</sub>:Mn single crystals, J. Appl. Phys. 114 (2013) 0-6, doi:10.1063/1.4821030.
- [12] K.H. Brosnan, S.F. Poterala, R.J. Meyer, S. Misture, G.L. Messing, Templated grain growth of <001>textured PMN-28PT using SrTiO<sub>3</sub> templates, J. Am. Ceram. Soc. 92 (2009) 133–139, doi:10.1111/j.1551-2916.2008.02628.x.
- [13] P. Li, Y. Huan, W. Yang, F. Zhu, X. Li, X. Zhang, B. Shen, J. Zhai, High-performance potassium-sodium niobate lead-free piezoelectric ceramics based on polymorphic phase boundary and crystallographic texture, Acta Mater 165 (2019) 486–495, doi:10.1016/j.actamat.2018.12.024.
- [14] L. Bian, X. Qi, K. Li, Y. Yu, L. Liu, Y. Chang, W. Cao, S. Dong, Ferroelectric Ceramics for Electromechanical Coupling Devices, Adv. Funct. Mater. 3 (2020) 1–7, doi:10.1002/adfm.202001846.
- [15] Y. Liu, Y. Chang, E. Sun, F. Li, S. Zhang, B. Yang, Y. Sun, J. Wu, W. Cao, Significantly enhanced energy-harvesting performance and superior fatigue-resistant behavior in [001]c-Textured BaTiO<sub>3</sub>-based lead-free Piezoceramics, ACS Appl. Mater. Interfaces. 10 (2018) 31488–31497, doi:10.1021/acsami.8b10361.
- [16] Y. Yan, Y.U. Wang, S. Priya, Electromechanical behavior of [001]-textured Pb(Mg<sub>1/3</sub>Nb<sub>2/3</sub>)O<sub>3</sub>-PbTiO<sub>3</sub> ceramics, Appl. Phys. Lett. 100 (2012), doi:10.1063/ 1.4712563.
- [17] Y. Yan, K.H. Cho, D. Maurya, A. Kumar, S. Kalinin, A. Khachaturyan, S. Priya, Giant energy density in [001]-textured Pb(Mg<sub>1/3</sub>Nb<sub>2/3</sub>)O<sub>3</sub>-PbZrO<sub>3</sub>-PbTiO<sub>3</sub> piezoelectric ceramics, Appl. Phys. Lett. 102 (2013) 1–6, doi:10.1063/1.4789854.
- [18] B.H. Watson, M.J. Brova, Y. Chang, S.T. Misture, M.A. Fanton, R.J. Meyer, G.L. Messing, Low temperature reactive sintering of CuO-doped PIN-PMN-PT ceramics, J. Eur. Ceram. Soc. 39 (2019) 4719–4726, doi:10.1016/j.jeurceramsoc. 2019.06.030.
- [19] Y. Yan, K.H. Cho, S. Priya, Piezoelectric properties and temperature stability of Mn-doped Pb(Mg<sub>1/3</sub>Nb<sub>2/3</sub>)-PbZrO<sub>3</sub>-PbTiO<sub>3</sub> textured ceramics, Appl. Phys. Lett. 100 (2012), doi:10.1063/1.3698157.
- [20] S.F. Poterala, S. Trolier-Mckinstry, R.J. Meyer, G.L. Messing, Processing, texture quality, and piezoelectric properties of 001 C textured (1-x)Pb(Mg<sub>1/3</sub>Nb<sub>2/3</sub>)TiO<sub>3</sub>-xPbTiO<sub>3</sub> ceramics, J. Appl. Phys. 110 (2011), doi:10.1063/1.3603045.
- [21] E.M. Sabolsky, S. Trolier-McKinstry, G.L. Messing, Dielectric and piezoelectric properties of ⟨001⟩ fiber-textured 0.675Pb(Mg<sub>1/3</sub>Nb<sub>2/3</sub>)O<sub>3</sub>-0.325PbTiO<sub>3</sub> ceramics, J. Appl. Phys. 93 (2003) 4072-4080, doi:10.1063/1.1554488.

[22] H. Liu, Y. Yan, H. Leng, A. Heitmann, J.B. Blottman, S. Priya, High performance high power textured piezoceramics, Appl. Phys. Lett. 116 (2020), doi:10.1063/ 5.0009501.

- [23] S. Su, R. Zuo, D. Lv, J. Fu, Synthesis and characterization of (001) oriented BaTiO<sub>3</sub> platelets through a topochemical conversion, Powder Technol 217 (2012) 11–15. doi:10.1016/j.powtec.2011.09.045.
- [24] H. Zhang, Y. Zhu, P. Fan, M.A. Marwat, W. Ma, K. Liu, H. Liu, B. Xie, K. Wang, J. Koruza, Temperature-insensitive electric-field-induced strain and enhanced piezoelectric properties of <001>textured (K,Na)NbO<sub>3</sub>-based lead-free piezoceramics, Acta Mater 156 (2018) 389–398, doi:10.1016/j.actamat.2018.07.005.
- [25] F.K. Lotgering, Topotactical reactions with ferrimagnetic oxides having hexagonal crystal structures-II, J. Inorg. Nucl. Chem. 16 (1960) 100–108 https://doi.org/10.1016/0022-1902(60)80092-9.
- [26] M. Nord, P.E. Vullum, I. Maclaren, T. Tybell, R. Holmestad, Atomap: a new software tool for the automated analysis of atomic resolution images using two – dimensional Gaussian fitting, Adv. Struct. Chem. Imaging. (2017), doi:10.1186/s40679-017-0042-5.
- [27] H.Y. Park, C.H. Nam, I.T. Seo, J.H. Choi, S. Nahm, H.G. Lee, K.J. Kim, S.M. Jeong, Effect of MnO<sub>2</sub> on the piezoelectric properties of the 0.75Pb(Zr<sub>0.47</sub>Ti<sub>0.53</sub>)O<sub>3</sub>-0.25Pb(Zn<sub>1/3</sub>Nb<sub>2/3</sub>)O<sub>3</sub> ceramics, J. Am. Ceram. Soc. 93 (2010) 2537–2540, doi:10.1111/j.1551-2916.2010.03888.x.
- [28] B.H. Watson, M.J. Brova, M.A. Fanton, R.J. Meyer, G.L. Messing, Mn- and Mn/Cu-doped PIN-PMN-PT piezoelectric ceramics for high-power transducers, J. Am. Ceram. Soc. 103 (2020) 6319–6329, doi:10.1111/jace.17347.
- [29] P.W. Ruhrig, S. Trolier-McKinstry, S.E. Park, G.L. Meaaing, Dielectric and electromechanical properties of barium titanate single crystals grown by templated grain growth, IEEE Trans. Ultrason. Ferroelectr. Freq. Control. 47 (2000) 895–902, doi:10.1109/58.852072.
- [30] T. Takenaka, H. Nagata, Y. Hiruma, Y. Yoshii, K. Matumoto, Lead-free piezoelectric ceramics based on perovskite structures, J. Electroceramics. 19 (2007) 259–265, doi:10.1007/s10832-007-9035-4.
- [31] G.A. Rossetti, A.G. Khachaturyan, G. Akcay, Y. Ni, Ferroelectric solid solutions with morphotropic boundaries: vanishing polarization anisotropy, adaptive, polar glass, and two-phase states, J. Appl. Phys. 103 (2008), doi:10.1063/1. 2930883
- [32] Y.M. Jin, Y.U. Wang, A.G. Khachaturyan, J.F. Li, D. Viehland, Conformal miniaturization of domains with low domain-wall energy: Monoclinic ferroelectric states near the morphotropic phase boundaries, Phys. Rev. Lett. 91 (2003) 1-4, doi:10.1103/PhysRevLett.91.197601.
- [33] F. Li, S. Zhang, D. Damjanovic, L.Q. Chen, T.R. Shrout, Local structural heterogeneity and electromechanical responses of ferroelectrics: learning from Relaxor ferroelectrics, Adv. Funct. Mater 28 (2018) 1–21, doi:10.1002/adfm. 2018.015.04
- [34] I.K. Jeong, T.W. Darling, J.K. Lee, T. Proffen, R.H. Heffner, J.S. Park, K.S. Hong, W. Dmowski, T. Egami, Direct observation of the formation of polar nanoregions in Pb(Mg<sub>1/3</sub>Nb<sub>2/3)</sub>O<sub>3</sub> using neutron pair distribution function analysis, Phys. Rev. Lett. 94 (2005) 1–4, doi:10.1103/PhysRevLett.94.147602.

- [35] F. Li, S. Zhang, T. Yang, Z. Xu, N. Zhang, G. Liu, J. Wang, J. Wang, Z. Cheng, Z.G. Ye, J. Luo, T.R. Shrout, L.Q. Chen, The origin of ultrahigh piezoelectricity in relaxor-ferroelectric solid solution crystals, Nat. Commun. 7 (2016) 1–9, doi:10. 1038/ncomms13807.
- [36] A. Kumar, J.N. Baker, P.C. Bowes, M.J. Cabral, S. Zhang, E.C. Dickey, D.L. Irving, J.M. LeBeau, Atomic-resolution electron microscopy of nanoscale local structure in lead-based relaxor ferroelectrics, Nat. Mater. 20 (2021) 62–67, doi:10.1038/s41563-020-0794-5.
- [37] F. Li, D. Lin, Z. Chen, Z. Cheng, J. Wang, C. Li, Z. Xu, Q. Huang, X. Liao, L.Q. Chen, T.R. Shrout, S. Zhang, Ultrahigh piezoelectricity in ferroelectric ceramics by design, Nat. Mater. 17 (2018) 349–354, doi:10.1038/s41563-018-0034-4.
- [38] C. Dagdeviren, P. Joe, O.L. Tuzman, K. Il Park, K.J. Lee, Y. Shi, Y. Huang, J.A. Rogers, Recent progress in flexible and stretchable piezoelectric devices for mechanical energy harvesting, sensing and actuation, Extrem. Mech. Lett. 9 (2016) 269–281, doi:10.1016/j.eml.2016.05.015.
- [39] D. Damjanovic, M. Budimir, M. Davis, N. Setter, Piezoelectric anisotropy: Enhanced piezoelectric response along nonpolar directions in perovskite crystals, J. Mater. Sci. 41 (2006) 65–76, doi:10.1007/s10853-005-5925-5.
- [40] X. Liu, S. Zhang, J. Luo, T.R. Shrout, W. Cao, A complete set of material properties of single domain 0.26Pb(In<sub>1/2</sub>Nb<sub>1/2</sub>)O<sub>3</sub>-0.46Pb(Mg<sub>1/3</sub>Nb<sub>2/3</sub>)O<sub>3</sub>-0.28PbTiO<sub>3</sub> single crystals, Appl. Phys. Lett. 96 (2010) 2008–2011, doi:10.1063/1.3275803.
- [41] S. Gupta, A. Belianinov, M. Baris Okatan, S. Jesse, S.V. Kalinin, S. Priya, Fundamental limitation to the magnitude of piezoelectric response of (001)pc textured K<sub>0.5</sub>Na<sub>0.5</sub>NbO<sub>3</sub> ceramic, Appl. Phys. Lett. 104 (2014) 0–5, doi:10.1063/1.4874648
- [42] X. Ren, Large electric-field-induced strain in ferroelectric crystals by point-defect-mediated reversible domain switching, Nat. Mater. 3 (2004) 91–94, doi:10.1038/nmat1051.
- [43] W.L. Warren, K. Vanheusden, D. Dimos, G.E. Pike, B.A. Tuttle, Oxygen vacancy motion in perovskite oxides, J. Am. Ceram. Soc. 79 (1996) 536–538, doi:10. 1111/j.1151-2916.1996.tb08162.x.
- [44] L. Zheng, L. Yang, Y. Li, X. Lu, D. Huo, W. Lü, R. Zhang, B. Yang, W. Cao, Origin of Improvement in Mechanical Quality Factor in Acceptor-Doped Relaxor-Based Ferroelectric Single Crystals, Phys. Rev. Appl. 9 (2018) 64028, doi:10.1103/PhysRevApplied.9.064028.
- [45] G. Liu, S. Zhang, W. Jiang, W. Cao, Losses in ferroelectric materials, Mater. Sci. Eng. R Reports. 89 (2015) 1–48, doi:10.1016/j.mser.2015.01.002.
- [46] J.J. Wang, B. Wang, L.Q. Chen, Understanding, Predicting, and Designing Ferroelectric Domain Structures and Switching Guided by the Phase-Field Method, Annu. Rev. Mater. Res. 49 (2019) 127–152, doi:10.1146/annurev-matsci-070218-121843.
- [47] N. Khakpash, H. Khassaf, G.A. Rossetti, S.P. Alpay, Misfit strain phase diagrams of epitaxial PMN-PT films, Appl. Phys. Lett. 106 (2015), doi:10.1063/1.4913706.
- [48] C. Yang, E. Sun, B. Yang, W. Cao, Theoretical study on local domain pinning effect due to defect dipole alignment, J. Phys. D. Appl. Phys. 51 (2018), doi:10. 1088/1361-6463/aadcd4.